materials

MDPI

Article

The Effect of Lithium Doping on the Sintering and Grain Growth of SPS-Processed, Non-Stoichiometric Magnesium Aluminate Spinel

Yuval Mordekovitz †, Lee Shelly †, Mahdi Halabi, Sergey Kalabukhov and Shmuel Hayun *

Department of Materials Engineering, Ben-Gurion University of the Negev, P.O. Box 653, Beer-Sheva 8410501, Israel; yuvalmor@post.bgu.ac.il (Y.M.); leeshel@post.bgu.ac.il (L.S.); mahdi@post.bgu.ac.il (M.H.); kalabukh@bgu.ac.il (S.K.)

* Correspondence: hayuns@bgu.ac.il; Tel.: +972-8-642-8742; Fax: +972-8-642-8744

† These authors contributed equally to this work.

Academic Editor: Eugene A. Olevsky

Received: 11 May 2016; Accepted: 7 June 2016; Published: 16 June 2016

Abstract: The effects of lithium doping on the sintering and grain growth of non-stoichiometric nano-sized magnesium aluminate spinel were studied using a spark plasma sintering (SPS) apparatus. Li-doped nano-MgO· $n$$Al_2O_3$ spinel (n = 1.06 and 1.21) powders containing 0, 0.20, 0.50 or 1.00 at. % Li were synthesized by the solution combustion method and dense specimens were processed using a SPS apparatus at 1200 °C and under an applied pressure of 150 MPa. The SPS-processed samples showed mutual dependency on the lithium concentration and the alumina-to-magnesia ratio. For example, the density and hardness values of near-stoichiometry samples (n = 1.06) showed an incline up to 0.51 at. % Li, while in the alumina rich samples (n = 1.21), these values remained constant up to 0.53 at. % Li. Studying grain growth revealed that in the Li-MgO· $n$$Al_2O_3$ system, grain growth is limited by Zener pining. The activation energies of undoped, 0.2 and 0.53 at. % Li-MgO· 1.21Al_2O_3 samples were 288 ± 40, 670 ± 45 and 543 ± 40 kJ· mol^{-1}, respectively.

Keywords: grain growth; lithium; magnesium aluminate spinel; precipitation; SPS

1. Introduction

Magnesium aluminate spinel (MgO· $n$$Al_2O_3$) is an attractive ceramic material for many technological applications, owing to its combination of excellent mechanical and optical properties [1–3]. To realize and maximize its qualities, the spinel must be sintered to full density. Sintering to full density is usually a difficult goal to achieve, given the requirements of high pressure and elevated temperatures. Yet, even then, variations in powder quality and densification processes can cause optical defects [4–6]. To overcome these issues, the use of sintering additives, such as Na_3AlF_6 [7], AlF_3 [3], B_2O_3 [8], $AlCl_3$ [3], CaO [2], LiF [9–11] and $CaCO_3$ + LiF [4], has been proposed. Of these, it was established that LiF consistently allowed for the sintering of transparent spinel [6,9–12]. As such, the effect of LiF on the sintering behavior of $MgAl_2O_4$ has been extensively studied [6,9–14], including by Meir *et al.* [10] and Rosenburg *et al.* [11].

Two mechanisms were proposed to explain the enhanced sintering kinetics and improved transparency attained by the sintered parts. The first involves the formation of a liquid phase (LiF, melting point (m.p.) ~847 °C) at relatively low temperature that wets the $MgAl_2O_4$ particles and likely aids densification by particle rearrangement and liquid-phase sintering. The second mechanism was proposed to act at higher temperatures. Here, LiF decomposes and the highly reactive F^- ions react with impurities (e.g., C and S), thereby cleaning/activating particle surfaces. In turn, the Li^+ cations react with the spinel, resulting in accelerated mass transport due to the formation of

oxygen vacancies. Recently, we studied the effects of lithium on the energetics, thermal stability, and coarsening of $MgO\cdot nAl_2O_3$, as well as its solubility in two-alumina-rich spinel compositions (n = 1.06 and n = 1.21). It was established that the phase stability of Li-doped, near-stoichiometry (n = 1.06) spinels is size-dependent. The spinel structure was able to hold up to 1 at. % lithium at grain sizes smaller than 30 nm, whereas for larger crystallite sizes, Mg(Li,Al)O and γ-$LiAlO_2$ phases precipitated. The aluminum-rich samples (n = 1.21) showed greater phase stability, with decomposition occurring only above 1 at. % lithium, independent of crystallite size. The measured surface (and interface) enthalpies of $MgO\cdot 1.06Al_2O_3$, $MgO\cdot 1.21Al_2O_3$ and 0.20 at. % Li-$MgO\cdot 1.21Al_2O_3$ were 1.51 $\pm$ 0.15 (0.42 $\pm$ 0.20) Jm^{-2}, 1.17 $\pm$ 0.15 (0.32 $\pm$ 0.21) and 1.05 $\pm$ 0.12 (0.24 $\pm$ 0.18) Jm^{-2}, respectively [15]. These values are in agreement with the lower coarsening tendency of aluminum-rich spinels [15]. Spark plasma sintering is a well-established method for sintering transparent magnesium aluminate spinel [10,16–24] which combines axial pressure with heating via an electrical current passing through a die containing the powder body. A LiF sintering additive (~1 wt. %) is typically required for transparency.

In the present work, dense bodies from various lithium-doped nano-$MgO\cdot 1.06Al_2O_3$ and $MgO\cdot 1.21Al_2O_3$ spinels were SPS-processed and their microstructure and phase composition were analyzed. The cardinal role of the Li additive is emphasized and discussed.

2. Materials and Experimental Procedures

Li-doped nano-$MgO\cdot nAl_2O_3$ spinel (n = 1.06 and 1.21) powders containing 0, 0.20, 0.50 or 1.00 at. % Li were synthesized by the solution combustion method [25], as described in detail by Mordekovitz and Hayun [15]. A 100 mL water-based solution was prepared with the appropriate amount of magnesium nitrate ($Mg(NO_3)_2\cdot 6H_2O$, 96% metal basis, Fluka Analytical, St. Louis, MO, USA), aluminum nitrate ($Al(NO_3)_3\cdot 9H_2O$, 96% metal basis, Fluka Analytical) and lithium acetate ($LiCH_3CO_2\cdot 2H_2O$, reagent grade, metal basis, Alfa Aesar, Haverhill, MA, USA). Thirty-seven grams of citric acid (ACS reagent $\geqslant$99.5) and 6 mL ethylene glycol (anhydrous, 99.8%, Sigma Aldrich, St. Louis, MO, USA) were added to the solution. The resulting mixtures were evaporated at 120 °C under agitation by magnetic stirring until high-viscosity foam-like colloids had formed. Finally, the dried gel precursor was calcined at 850 °C for 72 h to obtain a fine powder. Sintering was conducted in a Spark Plasma Sintering Machine (FCT Systems GmbH, Rauenstein, Germany) using a modified elevated pressure set-up capable of delivering uniaxial pressures greater than 500 MPa. Ten millimeter disks were sintered using a graphite die (20 mm outer diameter) with silicon carbide (SiC) plungers placed inside a conventional 20 mm graphite die-and-plunger set. All SPS experiments were conducted in a low vacuum (1.3 hPa), with a K-type control thermocouple in contact with the outer wall of the ø10 mm die. The sintering procedure was conducted at 1200 °C under 150–300 MPa of uniaxial pressure. The heating rate was 50 °C/min and the holding time at the highest temperature was 15 min. Grain growth heat treatments were performed in air for 8, 24 and 72 h at a temperature range of 1300–1450 °C. X-ray powder diffraction (XRD) was performed using a Rigaku RINT 2100 diffractometer with Cu Kα radiation (Tokyo, Japan). The operating parameters were 40 KV and 40 mA with a 2θ step of 0.02°. Cell parameters were calculated from the diffractions obtained using the MDI Jade 2010 software package (version 2.8.1, 2014, Materials Data, Livermore, CA, USA).

Microstructure was studied using high-resolution scanning electron microscopy (HRSEM, JEOL-7400F, Tokyo, Japan) and by transmission electron microscopy (TEM) using a JEOL 2100 (Tokyo, Japan) microscope equipped with a high-angle annular dark-field (HAADF) GATAN detector. Samples for scanning electron microscope (SEM) characterization were prepared using a standard metallographic procedure, finalized by polishing with a 1 µm diamond paste. Polished specimens were thermally etched at the same heat treatment temperature for 6 min.

TEM and STEM (scanning transmission electron microscope) samples were prepared from a copper-matrix composite with the spinel samples being embedded in the soft copper matrix, as described in detail by Halabi *et al.* [26] this technique was used in order to overcome charge-related

issues encountered during the TEM work. The spinel samples were ground and mixed with pure copper powder (~10 μm). Disks 3 mm in diameter and 70 μm thick were pressed and sintered at 700 °C in an N_2 atmosphere. The perforation stage was carried out using a Gatan Dimpler and Precision Ion Polishing System. Grain size was estimated using Thixomet software [27] for image analysis. The density of the specimens was measured by the Archimedes method (ASTM Standard B-311 [28]), while Vickers hardness was measured using a Buehler–Micromet 2100 hardness tester (2 kg load, ASTM Standard C-1327 [29]). The samples were polished to an optical level for transmission measurements at 500 and 1000 nm wavelengths (Spectrophotometer V-1100D, MRC, Holon, Israel).

3. Results and Discussion

3.1. Phase Composition

Figure 1 shows XRD patterns for Li-doped and undoped nano-crystalline $MgO\cdot 1.06Al_2O_3$ and $MgO\cdot 1.21Al_2O_3$ samples synthesized by the combustion synthesis technique. The patterns indicate the presence of a spinel phase with relatively broad reflection peaks, suggesting small crystallite sizes calculated to range between 9.2 ± 0.2 and 32.5 ± 0.6 nm in the pure and doped samples (Table 1). Detailed characterization of the nano-powders prepared by this method can be found elsewhere [15].

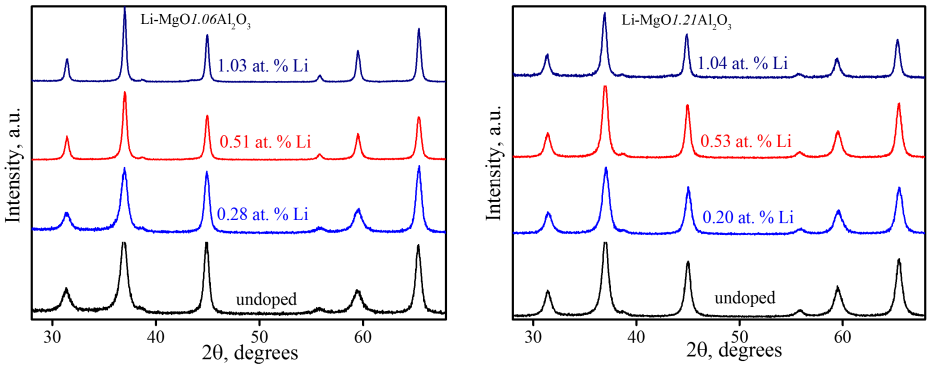

Figure 1. XRD patterns of as-synthesized powder samples.

Typical SPS-processed specimens from as-synthesized $MgO\cdot 1.06Al_2O_3$ powders containing different amounts of lithium are shown in Figure 2. The effect of lithium on the translucency of the $MgO\cdot 1.06Al_2O_3$ specimens is very apparent. In the present study, no attempts to determine optimal sintering conditions were made, with all of the compositions being sintered under the same conditions. The density, transmittance and hardness values (Table 1) of the samples prepared from near-stoichiometric powders (n = 1.06) all show maxima in the 0.51 at. % Li-$MgO\cdot 1.06Al_2O_3$ composition. Alumina-rich powders (n = 1.21) containing up to 0.53 at. % Li only reached about 95% of the theoretical density under these sintering conditions. Moreover, the samples showed no change in density, transmittance or hardness up to 0.53 at. % Li. At a higher lithium content (*i.e.*, 1.04 at. %), enhanced sinterability was observed.

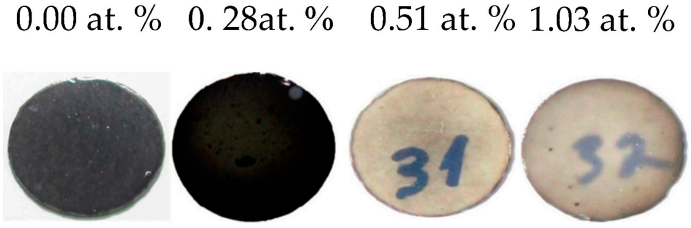

Figure 2. Photograph of Li-$MgO\cdot 1.06Al_2O_3$ SPS-processed samples. The polished specimens are 10 mm in diameter and ~1.5 mm thick. The effect of lithium on transparency is visible.

Table 1. Cell parameter grain size, density, transmittence, hardness and MgO s.s. amount for SPS-processed Li-doped MgO· $n$$Al_2O_3$ (n = 1.06 and 1.21) samples.

Li (at. %)	A (Å)	D (nm)	ρ (g/cm^3)	Trans. (500 nm) (%)	Trans. (1000 nm) (%)	Hardness (GPa)	$Mg_x(Al,Li)_{1-x}O$			
							Wt. %	*a* (Å)	Composition *	
									Mg	(Al, Li)
Li-MgO· 1.06Al_2O_3										
-	8.0810 (1)	102 ± 3	3.49 ± 0.01	-	-	14.3 ± 0.2	-	-	-	-
0.28 ± 0.02	8.0815 (1)	160 ± 5	3.54 ± 0.01	3.5 ± 0.1	14.4 ± 0.1	14.7 ± 0.3	0.9 ± 0.1	4.180 (9)	0.86	0.14
0.51 ± 0.05	8.0784 (1)	171 ± 3	3.56 ± 0.01	25.0 ± 0.1	45.3 ± 0.1	15.3 ± 0.4	1.8 ± 0.1	4.141 (9)	0.68	0.32
1.03 ± 0.10	8.0773 (1)	150 ± 8	3.54 ± 0.01	7.4 ± 0.1	22.9 ± 0.1	14.6 ± 0.5	2.9 ± 0.2	4.127 (9)	0.63	0.37
Li-MgO· 1.21Al_2O_3										
-	8.0647 (1)	81 ± 1	3.48 ± 0.01	-	-	14.4 ± 0.5	-	-	-	-
0.20 ± 0.02	8.0654 (1)	86 ± 2	3.49 ± 0.01	-	-	14.2 ± 0.2	-	-	-	-
0.53 ± 0.06	8.0656 (4)	94 ± 2	3.48 ± 0.01	-	-	14.1 ± 0.4	-	-	-	-
1.04 ± 0.10	8.0779 (2)	138 ± 4	3.61 ± 0.01	2.0 ± 0.1	10 ± 0.1	13.9 ± 0.3	2.3 ± 0.3	4.117 (9)	0.6	0.4

* Calculated using the Vegard rule and data from Doman's work [30].

The microstructures of the different SPS-processed specimens are presented in Figure 3. While the microstructure of the undoped MgO· $1.06Al_2O_3$ sample displayed a homogeneous nano-structure with equiaxed grains (Figure 3), the Li-doped samples consisted of two grain size populations. The doped and undoped MgO· $1.21Al_2O_3$ samples with lithium doping lower than 1.04 at. % seemed to be unaffected by the lithium addition and displayed similar equiaxed microstructures (Figure 3). The 1.04 at. % Li-MgO· $1.21Al_2O_3$ sample, however, showed a similar microstructure to the 1.03 at. % Li-MgO· $1.06Al_2O_3$ sample. The corresponding grain size distribution (an example is shown in Figure 4) exhibited a log-normal characteristic for all samples, with the calculated values summarized in Table 1. The grain size of near-stoichiometric specimens (n = 1.06) increased monotonically with the addition of lithium. However, this value appeared constant in alumina-rich powders (n = 1.21) containing up to 0.53 at. % Li. At higher lithium content (1.04 at. %), this value increased.

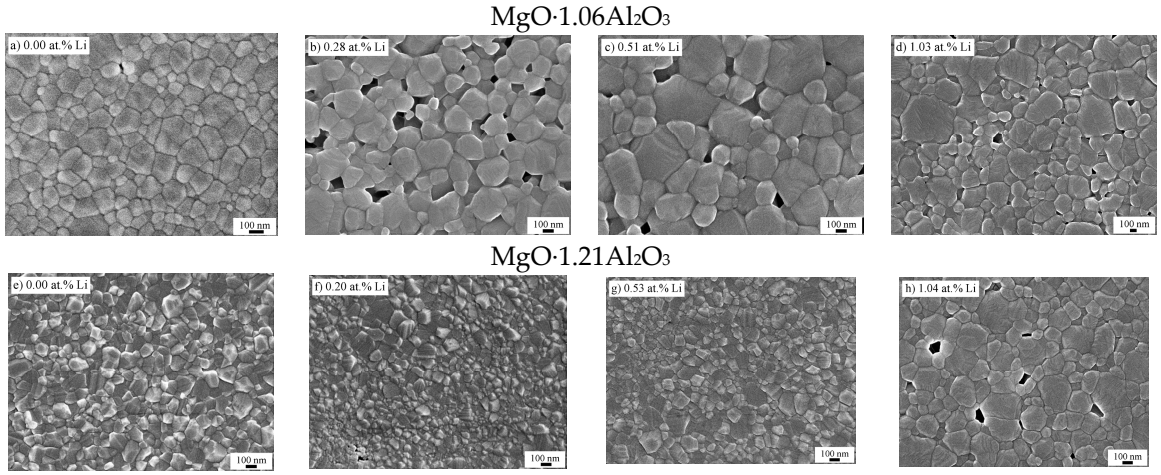

Figure 3. SEM micrographs of MgO· $1.06Al_2O_3$ and MgO· $1.21Al_2O_3$ SPS-processed samples. (**a**)–(**h**).

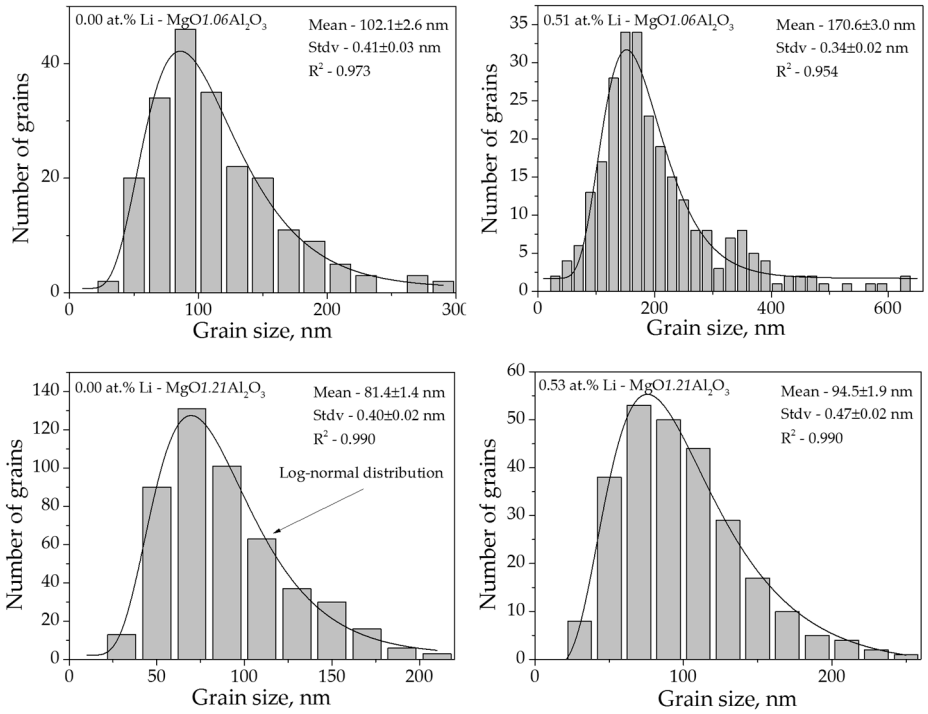

Figure 4. Typical grain size distribution and log-normal fitting of MgO· $1.06Al_2O_3$ and MgO· $1.21Al_2O_3$ with and without lithium addition processed by SPS.

The XRD patterns of the SPS-processed specimens are shown in Figure 5. The SPS-processed $MgO{\cdot}1.06Al_2O_3$ and 0.00–0.51 at. % Li-$MgO{\cdot}1.21Al_2O_3$ samples remained as a solid solution, while in the case of the 1.04 at. % Li-$MgO{\cdot}1.21Al_2O_3$ and 0.28 through 1.03 at. % Li-$MgO{\cdot}1.06Al_2O_3$ samples, Mg(Al,Li)O solid solution (MgO s.s.) and γ-$LiAlO_2$ [30,31] precipitated. The amounts of MgO s.s. precipitation were calculated using the Vegard rule and data from Reference [30] and are listed in Table 1. It should be noted that the γ-$LiAlO_2$ reflections were barely within the detection limit level of the XRD and were estimated to account for less than 1 wt. %. Similar behavior was found for the same powders after annealing at 1350 °C for 8 min in air [15].

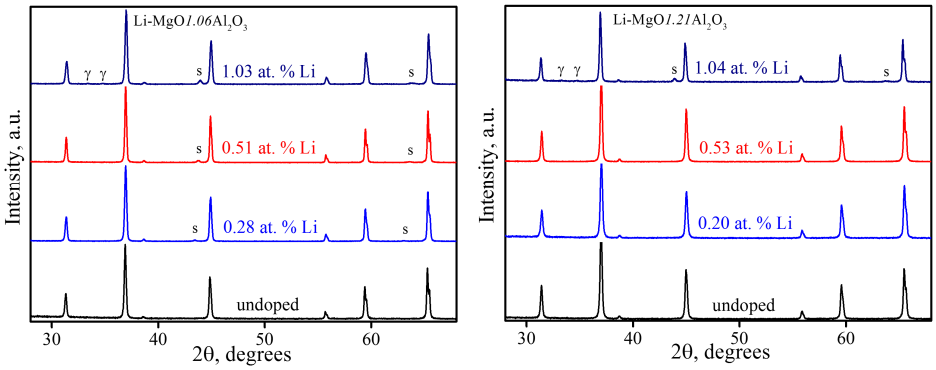

Figure 5. XRD patterns of Li-doped $MgO{\cdot}nAl_2O_3$ (n = 1.06 and 1.21) SPS-processed samples. The precipitated MgO s.s. and γ-$LiAlO_2$ phases are marked by s and γ, respectively.

In general, for samples containing up to 53.0 at. % Li, the cell parameters were 8.0810 ± 0.0005 Å and 8.0652 ± 0.0005 Å for n = 1.06 and 1.21, respectively. At higher Li content, both 1.03 at. % Li-$MgO{\cdot}1.06Al_2O_3$ and 1.04 at. % Li-$MgO{\cdot}1.21Al_2O_3$ samples displayed the same cell parameter (8.0776 ± 0.0004 Å).

3.2. Grain Growth

The undoped, 0.28 and 0.53 at. % Li-doped $MgO{\cdot}1.21Al_2O_3$ SPS-processed samples remained as a solid solution, all the while exhibiting homogeneous microstructures with equiaxed polyhedral-shaped grains. To reveal the effect of lithium on grain growth mechanisms, the grain sizes resulting from a set of heat treatments at various temperatures and times were measured (Table 2, Figure 6).

Table 2. Grain sizes of heat-treated, undoped and 0.28 and 0.53 at. % Li-doped $MgO{\cdot}1.21Al_2O_3$ samples.

Temperature (°C)/Time (h)	Grain Size (nm)		
	8	24	72
	$MgO{\cdot}1.21Al_2O_3$		
1300	105 ± 8	125 ± 10	229 ± 6
1375	131 ± 10	200 ± 19	272 ± 26
1450	181 ± 12	292 ± 26	513 ± 22
	0.28-$MgO{\cdot}1.21Al_2O_3$		
1300	111 ± 5	147 ± 10	157 ± 7
1375	154 ± 5	242 ± 18	249 ± 18
1450	306 ± 11	438 ± 9	991 ± 115
	0.53-$MgO{\cdot}1.21Al_2O_3$		
1300	113 ± 8	116 ± 5	201 ± 7
1375	149 ± 8	237 ± 53	280 ± 8
1450	197 ± 18	300 ± 6	948 ± 47

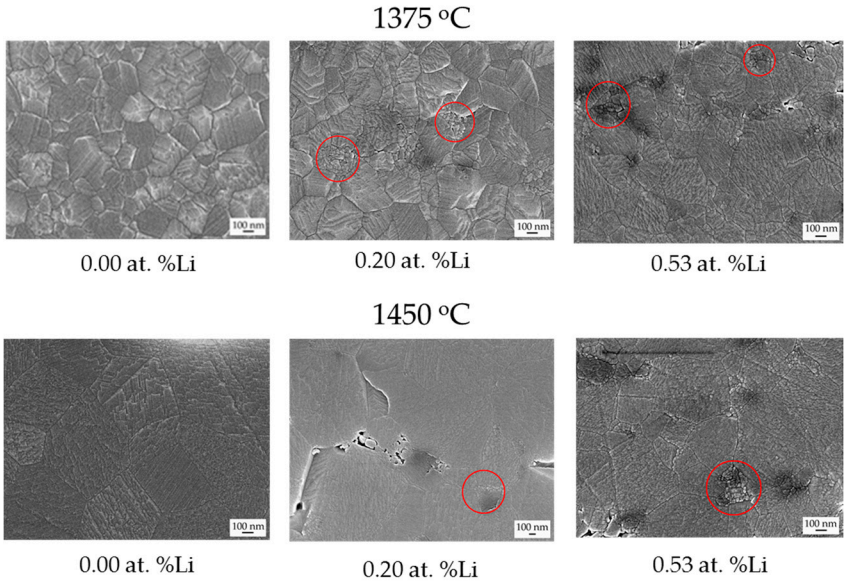

Figure 6. Micrographs of the undoped, 0.2 and 0.53 at. % Li-doped MgO· $1.21Al_2O_3$ samples after heat-treatment at 1375 and 1450 °C for 24 h. The presence of the fine grain clusters is marked by red circles.

The undoped MgO· $1.21Al_2O_3$ sample showed monotonic grain growth with temperature and time. The lithium-doped samples, however, presented a more complex behavior. At low temperatures and short holding times, the lithium-doped samples showed a monotonic-like behavior similar to the undoped samples. At higher temperatures (*i.e.*, 1450 °C, 8 h) or longer dwelling periods (*i.e.*, 1300 °C, 24 h), the 0.53 at. % Li-MgO· $1.21Al_2O_3$ sample displayed lesser growth than the 0.20 at. % Li-MgO· $1.21Al_2O_3$ sample (Figure 6). After a longer thermal exposure, namely 72 h at 1450 °C (Figure 6), the doped samples showed enhanced grain growth, reaching a size double that of the undoped sample.

Closer examination of the SEM images of the samples after heat treatment for 24 h at 1375 and 1450 °C (Figure 6) revealed the presence of small clusters of fine grains between larger grains in the doped samples. This finding suggests that lithium-rich phases may have precipitated during the heat treatments, which could explain the growth behavior of the doped samples.

Unfortunately, XRD analysis of these samples indicated only the presence of a spinel phase (Figure 7). Although no second phase was found, it might still be present, but it would remain undetected by the XRD technique if the phase only had a minor vol % and nano-sized dimensions [32].

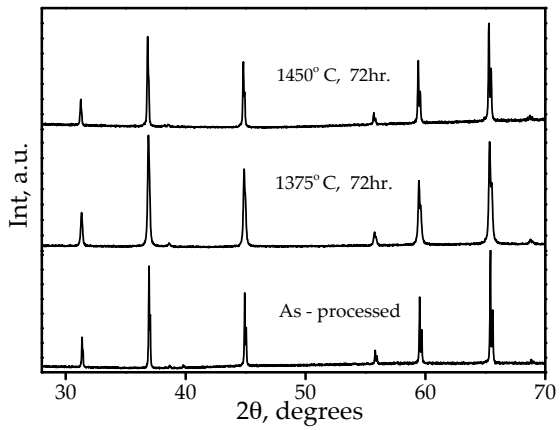

Figure 7. XRD spectra of as-processed and heat-treated to 1375 °C (72 h) and 1450 °C (72 h) samples.

To identify the nature of these fine grains, TEM analysis was performed on 0.20 at. % Li-MgO· $1.21Al_2O_3$ before and after heat treatment at 1450 °C for 24 and 72 h (Figure 8). The TEM image of the SPS-processed 0.20 at. % Li-MgO· $1.21Al_2O_3$ sample (Figure 8a) showed only spinel grains and confirmed the results of the XRD investigation regarding phase composition. After heat treatment at 1450 °C for 24 h, the presence of nano-particles of γ-lithium aluminate at the grain boundaries was detected (Figures 8b and 9).

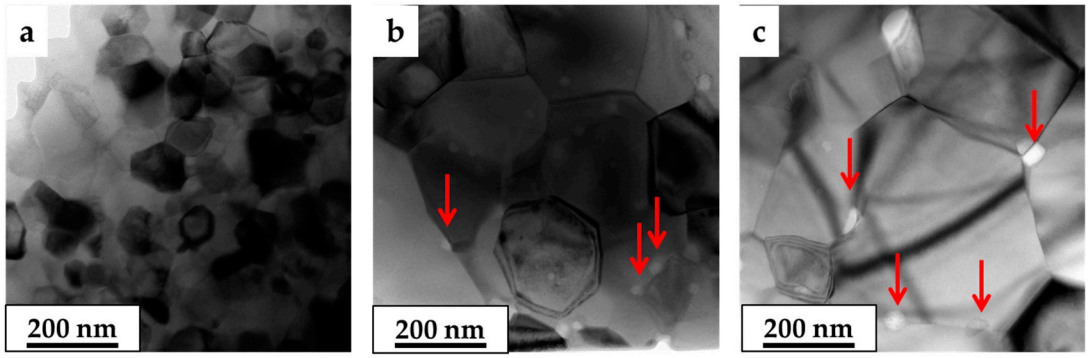

Figure 8. BF-TEM images of 0.20 at. % Li-MgO· $1.21Al_2O_3$ spinel system as-processed (**a**); heat-treated at 1450 °C for 24 h (**b**); and heat-treated at 1450 °C for 72 h (**c**). Second phase in grain boundary, especially in triple points, is clearly visible in the heat-treated samples.

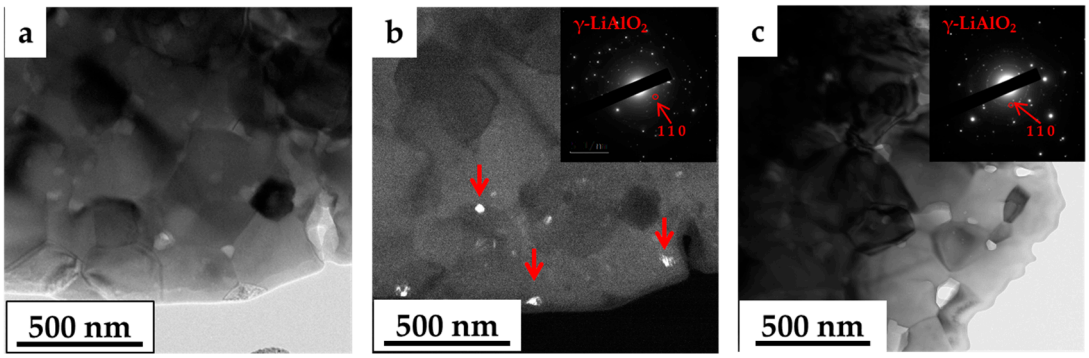

Figure 9. BF-TEM image of SPS spinel samples doped with 0.20 at. % Li after heat treatment at 1450 °C for 24 h (**a**); the white particles in the DF-TEM image are the γ-$LiAlO_2$ phase (**b**); BF-TEM image of spinel samples doped with 0.20 at. % Li after heat treatment at 1450 °C for 72 h (**c**); the selected area diffraction patterns indicate the reflection of (1 1 0) of the γ-$LiAlO_2$ phase.

In a previous study, we showed that the solubility limit of lithium in a spinel structure is controlled both by the Al-to-Mg ratio and by grain size [15]. Thus, even though no signs of second phase precipitation were present in the as-sintered 0.20 and 0.53 at. % Li-MgO· $1.21Al_2O_3$ samples, additional grain growth would promote lithium segregation to the grain boundaries and precipitation of a second phase. The segregation of lithium to the grain boundary increases the grain growth rate by reducing the grain boundary energy [15]. On the other hand, second phase precipitation impedes grain growth via the Zener pinning mechanism [33–36]. Such behavior can be seen in Figure 10. The 0.2 at. % Li-MgO· $1.21Al_2O_3$ spinel shows enhanced grain growth up to 24 h (<D> ~140 nm), after which time the growth is inhibited for a prolonged period of annealing due to second phase precipitation. In the more Li-rich samples (*i.e.*, 0.53 at. % Li), grain growth was inhibited at an early stage due to earlier second phase appearance. Further coarsening was related to precipitate coarsening followed by the grain coarsening [36].

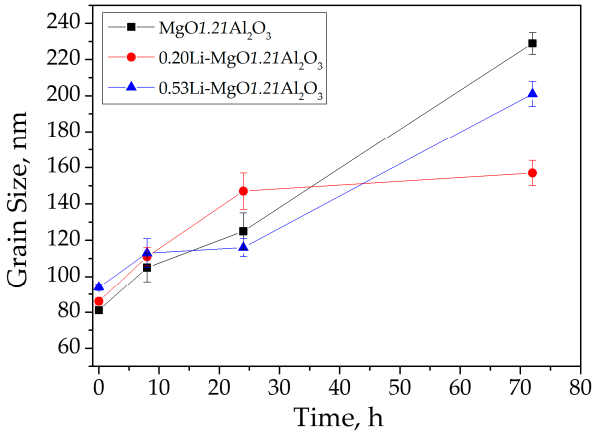

Figure 10. Grain sizes *vs.* annealing time of undoped, 0.2 and 0.53 at. % Li-doped MgO· $1.21Al_2O_3$ samples at 1300 °C.

Activation energy analysis of undoped, 0.2 and 0.53 at. % Li-doped MgO· $1.21Al_2O_3$ grain growth was performed using the phenomenological kinetic grain growth equation:

$$G_t^n - G_0^n = K_0 t exp\left(-\frac{Q}{RT}\right)$$

where G_t and G_0 are the grain sizes at times t and $t = 0$, respectively, n is the grain growth exponent, K_0 is the pre-exponential constant of the diffusion coefficient, Q is the activation energy for grain growth, T is the absolute temperature, and R is the gas constant.

The grain growth exponent or n value is readily determined as the inverse of the slope of a log G *vs.* log t plot. Using the original particle size as G_0, the grain size data can be fitted to linear lines with similar correlation factors ($R = 0.998$ and 0.937) for both the grain growth exponents of $n = 2$ (grain boundary–controlled diffusion) and $n = 3$ (lattice-controlled diffusion). This is in agreement with other works using either $n = 2$ or 3 [37,38]. Using $n = 2$, the activation energy and kinetic constant (K_0) for undoped MgO· $1.21Al_2O_3$ were found to be 288 ± 40 kJ· mol^{-1} and 2.09×10^6 $\mu m^2/h$. These values are in agreement with other data and are found between the values for $MgAl_2O_4$ and MgO· $1.56Al_2O_3$ (Table 3). The activation energies and K_0 for 0.2 and 0.53 at. % Li-MgO· $1.21Al_2O_3$ were found to be 670 ± 45, 543 ± 40 kJ· mol^{-1} and 3.41×10^{18}, 3.78×10^{14} $\mu m^2/h$, respectively; these values are significantly higher than those of the undoped sample. These findings are in line with the effect of the Zener pining mechanism, where grain growth is impeded at early stages by the secondary phase. Once the secondary phase has grown and the impediment is lifted, the spinel grains show enhanced growth (see data in Table 2) that can be attributed to the effect of lithium on the diffusion, by way of imposing oxygen vacancies [9–11,15].

Table 3. Grain growth parameters for 0–0.53 at. % Li-MgO· $1.21Al_2O_3$.

MgO· nAl_2O_3	Activation Energy for Grain Growth (kJ/mol)	ln(K_0)
	Undoped	
1.56 (Chiang [39])	248 ± 29	16.35
1.21 (This study)	288 ± 40	14.55
1.013 (Chiang [39])	422 ± 10	28.23
~1.00 (Bratton [40])	462	30.54
at. % Li	Lithium doped $n = 1.21$ (This study)	
0.20	670 ± 45	42.67
0.53	543 ± 40	33.56

4. Summary

The effects of lithium doping on the sintering and grain growth kinetics of non-stoichiometric nano-MgO· $n$$Al_2O_3$ spinel with n = 1.06 and 1.21 were studied using a spark plasma sintering apparatus. The near-stoichiometry (n = 1.06) Li-doped samples showed higher sinterability in comparison with the aluminum-rich samples (n = 1.21) but also lower phase stability, with Mg(Li,Al)O and γ-$LiAlO_2$ phases precipitating during the course of the sintering process. Still, the aluminum-rich system (n = 1.21) showed greater phase stability up to 1 at. % of lithium for samples with grain sizes lower than 100 nm. The grain growth study indicated that in the Li-MgO· $n$$Al_2O_3$ system, grain growth was controlled by the Zener pining mechanism, where γ-$LiAlO_2$ precipitated at the grains boundaries. The activation energies of the undoped, 0.20 and 0.53 at. % Li-MgO· 1.21Al_2O_3 samples were 288 ± 40, 670 ± 45 and 543 ± 40 kJ· mol^{-1}, respectively.

Acknowledgments: This work was partially supported by the FP7-PEOPLE-2012-CIG (grant 321838-EEEF-GBE-CNS).

Author Contributions: Yuval Mordekovitz was responsible for the literature review, prepared samples for characterization, analyzed microstructural images and XRD patterns, and processed the experimental data. Lee Shelly performed the grain growth experiments, analyzed the grain growth data and interpreted the results. Mahdi Halabi prepared and executed the TEM experiments, analyzed the data and interpreted the results. Sergey Kalabukhov fabricated samples by SPS. Shmuel Hayun supervised the work and interpreted the results. All authors contributed to the writing of the paper.

Conflicts of Interest: The authors declare no conflict of interest.

Abbreviations

The following abbreviations are used in this manuscript:

SPS	spark plasma sintering
HRSEM	high resolution scanning electron microscope
HRTEM	high resolution transmission electron microscope
HAADF	high angle annular dark field
STEM	scanning transmission electron microscope
XRD	X-ray powder diffraction
MgO s.s.	Mg(Al,Li)O solid solution
BF-TEM	bright field transmission electron microscope
DF-TEM	dark field transmission electron microscope

References

1. Goldstein, A. Correlation between $MgAl_2O_4$-spinel structure, processing factors and functional properties of transparent parts (progress review). *J. Eur. Ceram. Soc.* **2012**, *32*, 2869–2886. [CrossRef]
2. Ganesh, I.; Teja, K.A.; Thiyagarajan, N.; Johnson, R.; Reddy, B.M. Formation and densification behavior of magnesium aluminate spinel: The influence of CaO and moisture in the precursors. *J. Am. Ceram. Soc.* **2005**, *88*, 2752–2761. [CrossRef]
3. Ganesh, I.; Bhattacharjee, S.; Saha, B.P.; Johnson, R.; Mahajan, Y.R. A new sintering aid for magnesium aluminate spinel. *Ceram. Int.* **2001**, *27*, 773–779. [CrossRef]
4. Huang, J.L.; Sun, S.Y.; Chen, C.Y. Investigation of high alumina-spinel: Effects of LiF and $CaCO_3$ addition (part 2). *Mater. Sci. Eng. A* **1999**, *259*, 1–7. [CrossRef]
5. Krell, A.; Hutzler, T.; Klimke, J.; Potthoff, A. Fine-grained transparent spinel windows by the processing of different nanopowders. *J. Am. Ceram. Soc.* **2010**, *93*, 2656–2666. [CrossRef]
6. Du Merac, M.R.; Reimanis, I.E.; Smith, C.; Kleebe, H.-J.; Müller, M.M. Effect of impurities and LiF additive in hot-pressed transparent magnesium aluminate spinel. *Int. J. Appl. Ceram. Technol.* **2013**, *10*, E33–E48. [CrossRef]
7. Chen, S.-K.; Cheng, M.-Y.; Lin, S.-J. Reducing the sintering temperature for MgO-Al_2O_3 mixtures by addition of cryolite (Na_3AlF_6). *J. Am. Ceram. Soc.* **2004**, *85*, 540–544. [CrossRef]
8. Bhattacharya, G.; Zhang, S.; Smith, M.E.; Jayaseelan, D.D.; Lee, W.E. Mineralizing magnesium aluminate spinel formation with B_2O_3. *J. Am. Ceram. Soc.* **2006**, *89*, 3034–3042. [CrossRef]

9. Rozenburg, K.; Reimanis, I.E.; Kleebe, H.-J.; Cook, R.L. Chemical interaction between LiF and $MgAl_2O_4$ spinel during sintering. *J. Am. Ceram. Soc.* **2007**, *90*, 2038–2042. [CrossRef]
10. Meir, S.; Kalabukhov, S.; Froumin, N.; Dariel, M.P.; Frage, N. Synthesis and densification of transparent magnesium aluminate spinel by SPS processing. *J. Am. Ceram. Soc.* **2009**, *92*, 358–364. [CrossRef]
11. Rozenburg, K.; Reimanis, I.E.; Kleebe, H.-J.; Cook, R.L. Sintering kinetics of a $MgAl_2O_4$ spinel doped with LiF. *J. Am. Ceram. Soc.* **2008**, *91*, 444–450. [CrossRef]
12. Du Merac, M.R.; Kleebe, H.-J.; Müller, M.M.; Reimanis, I.E. Fifty years of research and development coming to fruition; Unraveling the complex interactions during processing of transparent magnesium aluminate ($MgAl_2O_4$) spinel. *J. Am. Ceram. Soc.* **2013**, *96*, 3341–3365. [CrossRef]
13. Carnall, E. The densification of MgO in the presence of a liquid phase. *Mater. Res. Bull.* **1967**, *2*, 1075–1086. [CrossRef]
14. Reimanis, I.; Kleebe, H.-J. A review on the sintering and microstructure development of transparent spinel ($MgAl_2O_4$). *J. Am. Ceram. Soc.* **2009**, *92*, 1472–1480. [CrossRef]
15. Mordekovitz, Y.; Hayun, S. On the effect of lithium on the energetics and thermal stability of nano-sized nonstoichiometric magnesium aluminate spinel. *J. Am. Ceram. Soc.* **2016**. [CrossRef]
16. Morita, K.; Kim, B.-N.; Hiraga, K.; Yoshida, H. Fabrication of transparent $MgAl_2O_4$ spinel polycrystal by spark plasma sintering processing. *Scr. Mater.* **2008**, *58*, 1114–1117. [CrossRef]
17. Morita, K.; Kim, B.-N.; Yoshida, H.; Hiraga, K. Densification behavior of a fine-grained $MgAl_2O_4$ spinel during spark plasma sintering (SPS). *Scr. Mater.* **2010**, *63*, 565–568. [CrossRef]
18. Frage, N.; Cohen, S.; Meir, S.; Kalabukhov, S.; Dariel, M.P. Spark plasma sintering (SPS) of transparent magnesium-aluminate spinel. *J. Mater. Sci.* **2007**, *42*, 3273–3275. [CrossRef]
19. Morita, K.; Kim, B.-N.; Yoshida, H.; Hiraga, K. Spark-plasma-sintering condition optimization for producing transparent $MgAl_2O_4$ spinel polycrystal. *J. Am. Ceram. Soc.* **2009**, *92*, 1208–1216. [CrossRef]
20. Rothman, A.; Kalabukhov, S.; Sverdlov, N.; Dariel, M.P.; Frage, N. The effect of grain size on the mechanical and optical properties of spark plasma sintering-processed magnesium aluminate spinel $MgAl_2O_4$. *Int. J. Appl. Ceram. Technol.* **2014**, *11*, 146–153. [CrossRef]
21. Bonnefont, G.; Fantozzi, G.; Trombert, S.; Bonneau, L. Fine-grained transparent $MgAl_2O_4$ spinel obtained by spark plasma sintering of commercially available nanopowders. *Ceram. Int.* **2012**, *38*, 131–140. [CrossRef]
22. Fu, P.; Lu, W.; Lei, W.; Xu, Y.; Wang, X.; Wu, J. Transparent polycrystalline $MgAl_2O_4$ ceramic fabricated by spark plasma sintering: Microwave dielectric and optical properties. *Ceram. Int.* **2013**, *39*, 2481–2487. [CrossRef]
23. Morita, K.; Kim, B.-N.; Yoshida, H.; Zhang, H.; Hiraga, K.; Sakka, Y. Effect of loading schedule on densification of $MgAl_2O_4$ spinel during spark plasma sintering (SPS) processing. *J. Eur. Ceram. Soc.* **2012**, *32*, 2303–2309. [CrossRef]
24. Khasanov, O.; Dvilis, E.; Khasanov, A.; Polisadova, E.; Kachaev, A. Optical and mechanical properties of transparent polycrystalline $MgAl_2O_4$ spinel depending on SPS conditions. *Phys. Status Solidi* **2013**, *10*, 918–920. [CrossRef]
25. Ianoş, R.; Lazău, I.; Păcurariu, C.; Barvinschi, P. Solution combustion synthesis of $MgAl_2O_4$ using fuel mixtures. *Mater. Res. Bull.* **2008**, *43*, 3408–3415. [CrossRef]
26. Halabi, M.; (Ben-Gurion University of the Negev, Beer-Sheva, Israel). Personal communication, 2016.
27. Hayun, S.; Dilman, H.; Dariel, M.P.; Frage, N.; Dub, S. Effect of the carbon source on the microstructure and mechanical properties of reaction bonded boron carbide. In *Ceramic Transactions 209 (Advances in Sintering Science and Technology)*; American Ceramic Society: Westerville, OH, USA, 2010; pp. 29–41.
28. ASTM B-311. Standard test method for density of powder metallurgy (PM) materials containing less than two percent porosity 1. *ASTM Int.* **2008**. [CrossRef]
29. C-1327 A. Standard test method for vickers indentation hardness of advanced ceramics 1. *ASTM Int.* **2008**. [CrossRef]
30. Doman, R.C.; McNally, R.N. Solid solution studies in the MgO-LiAlO system. *J. Mater. Sci.* **1973**, *8*, 189–191. [CrossRef]
31. Izquierdo, G.; West, A.R. Compatibility relations in the system Li_2O-MgO-Al_2O_3. *J. Am. Ceram. Soc.* **1980**. [CrossRef]

32. Garitaonandia, J.S.; Gorria, P.; Barquín, L.F.; Barandiarán, J.M.; Barqu'in, L.F.; Barandiarán, J.M. Low-temperature magnetic properties of Fe nanograins in an amorphous Fe-Zr-B matrix. *Phys. Rev. B* **2000**, *61*, 6150–6155. [CrossRef]
33. Hassold, G.N.; Holm, E. Effects of particle size on inhibited grain growth. *Scr. Met. Mater.* **1990**, *24*, 11–13. [CrossRef]
34. Grewal, G.; Ankem, S. Modeling matrix grain growth in the presence of growing second phase particles in two phase alloys. *Acta Metall. Mater.* **1990**, *38*, 1607–1617. [CrossRef]
35. Fan, D.; Chen, L.-Q.; Chen, S.-P.P. Numerical simulation of zener pinning with growing second-phase particles. *J. Am. Ceram. Soc.* **1998**, *81*, 526–532. [CrossRef]
36. Rios, P.R. Overview no. 62. A theory for grain boundary pinning by particles. *Acta Metall.* **1987**, *35*, 2805–2814. [CrossRef]
37. Lappalainen, R.; Pannikkat, A.; Raj, R. Superplastic flow in a non-stoichiometric ceramic: Magnesium aluminate spinel. *Acta Metall. Mater.* **1993**, *41*, 1229–1235. [CrossRef]
38. Chaim, R. Activation energy and grain growth in nanocrystalline Y-TZP ceramics. *Mater. Sci. Eng. A* **2008**, *486*, 439–446. [CrossRef]
39. Chiang, Y. Grain boundary mobility and segregation in non-stoichiometric solid solutions of magnesium aluminate spinel. *J. Am. Ceram. Soc.* **1980**. [CrossRef]
40. Bratton, R.J. Sintering and grain-growth kinetics of something is missing here. *J. Eur. Ceram. Soc.* **1970**, *35*, 141–143.